CHAPTER 6

Photo-Fenton reaction on magnetite-GO nanocomposite: computational and experimental investigations

6.1 Introduction

The Fenton process is a green method that can degrade most organic pollutants in water using powerful hydroxyl radicals ($^{\bullet}OH$) oxidants [Zhang et al. (2019)]. The disadvantages of the conventional homogeneous Fenton process are narrow pH range, large sludge generation, and loss of reagents. These can be overcome by a heterogeneous Fenton-like process [Hussain et al. (2021), Wang et al. (2016)] which employs catalysts with sites or active centers having access to two oxidation states. Generally, the rate-limiting step of this cycle is also the back conversion of the catalyst active center from the oxidized to reduced state [Lyu et al. (2015), Song et al. (2006)]. The fabrication of catalysts with electron-rich and electron-deficient centers (or active sites) could be one of the ways of surmounting this disadvantage. While the electron-rich part could generate hydroxyl radicals by H_2O_2 reduction, the electron-deficient component can directly get electrons by organic pollutant oxidation.

Recently, Zhang and his co-workers [Zhang et al. (2021)] proposed from first-principle calculations that the two catalyst components in Fe_3O_4/rGO composite are connected via the bridging C-O-Fe interaction. In this composite, Fe_3O_4 and rGO act like dual electron centers. These electron centers support electron transfer and help dissociate H_2O_2. Another researcher, Lyu et al. (2016) fabricated d-TiCuAl-SiO_2 nanospheres (dandelion-like silica nanospheres) consisting of electron-rich and electron-deficient centers. They proposed Cu as electron-rich center atoms, which facilitates the reduction of H_2O_2 to $^{\bullet}OH$ around. Thus, the construction of composite catalysts with electron-rich and electron-deficient parts could enhance the Fenton process.

Chapters 4 and 5 have investigated the other requirements for fabricating an effective Fenton or photo-Fenton catalyst. Results of chapter 4 have demonstrated that H_2O_2 and the target organic pollutant molecules should be nearby because the generated

•OH radical has a short lifetime. Chapter 5 shows that the adsorption of the substrate (to be reduced) on nucleophilic sites of the catalyst is necessary for effective Fenton activity. Similarly, the molecule to be oxidized should interact effectively with the electrophilic portion of the catalyst. Furthermore, effective photocatalysis necessitates the fulfillment of the same requirements. The excited state HOMO (or nucleophilic portion) should have a particular affinity for the species to be reduced. Likewise, the LUMO of the excited photocatalyst should interact with the species to be oxidized. Thus, Chapter 5 of this thesis concluded the generation of •OH by H_2O_2 bond reduction requires effective interaction with the nucleophilic part of the catalyst HOMO.

The present chapter's objective is to understand the mechanism of the Fenton and photo-Fenton degradation of PNP on a magnetite-GO composite (MGO). The study is different from reference [Liu et al. (2019), Zubir et al. (2015)] because the present study also investigates the photo-Fenton properties of this composite. Thus, the GO part incorporated in the MGO composite has a visible bandgap. Furthermore, as in chapters 4 and 5, MD and DFT studies are undertaken to elucidate the mechanistic issues due to interfacial phenomena and the catalyst/photocatalyst electronic structure. The MGO composite was synthesized via a co-precipitation method.

The prepared MGO nanocomposite was characterized and used as a catalyst and a photocatalyst for PNP degradation. DFT was performed on the magnetite-graphene oxide model and TD-DFT calculations to calculate the excitation energies on the optimized model. Frontier molecular orbital theory was applied to find out HOMO and LUMO locations on the catalyst to check the nucleophilic site of the catalyst. The natural bond analysis (NBO) was carried out on the optimized MGO model to see the charge transfer. Then classical MD simulations gave information about how PNP and H_2O_2 molecules adsorb on MGO in the presence of many water molecules. Lastly,

experimental, MD, DFT, and TD-DFT results were combined to derive the suitable mechanism.

6.2 Experimental

6.2.1 Synthesis of Graphene Oxide (GO)

Modified Hummer's method was used to synthesize the graphene oxide nanosheets [Yeh et al. (2011)]. Typically, 2.5g of graphite powder (Sigma Aldrich) and 1.25g of $NaNO_3$ (Merck) were added to 60 ml of concentrated H_2SO_4 (18M) in the beaker over an ice bath. Subsequently, $KMnO_4$ (7g) was added gently under the stirring, maintaining the temperature below 20^oC. Then the solution temperature was increased to 35^oC and maintained at this temperature under stirring for 4 hours. The mixture was heated at 98^oC for 15 minutes with the gradual addition of 115 ml of distilled water. This suspension was further diluted by adding 350ml of distilled water. Next, 6ml of H_2O_2 was introduced to the above-diluted solution under vigorous stirring at 25^oC, and the reaction was stopped. The prepared sample was washed several times with distilled water and ethanol, dried at 60^oC for 24 hours.

6.2.2 Synthesis of Magnetite-Graphene oxide (MGO) composite

An appropriate amount of GO (5wt. %) was dispersed in 100 ml of distilled water by bath sonication for two hours. Next, an aqueous solution of iron (II) sulfate heptahydrate ($FeSO_4.7H_2O$, Merck) was mixed with the redispersed GO suspension. This mixture was added dropwise into a 0.4M NaOH solution at 80^oC from a burette under continuous stirring. The heating was continued (for two hours) until a dark black precipitate was formed. The precipitate was separated by magnetic decantation and then washed several times with distilled water and ethanol until the pH of water obtained after

washing became neutral. The precipitate was dried at 60°C for 24hour. A similar protocol was also followed for the synthesis of magnetite nanoparticles.

6.2.3 Catalytic Fenton and photo-Fenton experiment

For catalytic degradation analysis on prepared catalysts, 100µL dispersed catalyst (2mg in 2ml distlled water) was added to the 3ml of PNP solution at pH 3. This mixture was kept in the dark for one hour to complete adsorption. After that, 100µL diluted H_2O_2 solution (1M) was mixed with the above suspension. Two experiments were carried out, one in the dark and the other under visible light irradiation. The cool white LED (14W) was the visible light source for the photo-Fenton reaction.

6.3 Computational Methodology

6.3.1 DFT details

The GO1 model sheet, used in the DFT calculations, contains three hydroxyls, one epoxy, and one carboxylic acid functional group. The complete molecular formula of the GO1 model was $C_{54}H_{17}(O)_1(OH)_3(COOH)_1$. Note that this GO1 model is same as model (GOM1) which was used in chapter 5. Figure 6.1a shows a small Fe_3O_4 unit made by GaussView 6 software. The LANL2DZ for Fe atoms and the 6-31++g (d, p) basis sets for C, H, and O atoms were used to optimize the Fe_3O_4 unit and GO1 sheet [Rajeevgandhi et al. (2020)] separately. In both cases, the B3LYP (Becke-3-Parameter-Lee-Yang-Parr) functional was used for ground-state DFT calculations on Gaussian 16 software [Frisch et al. (2016)].

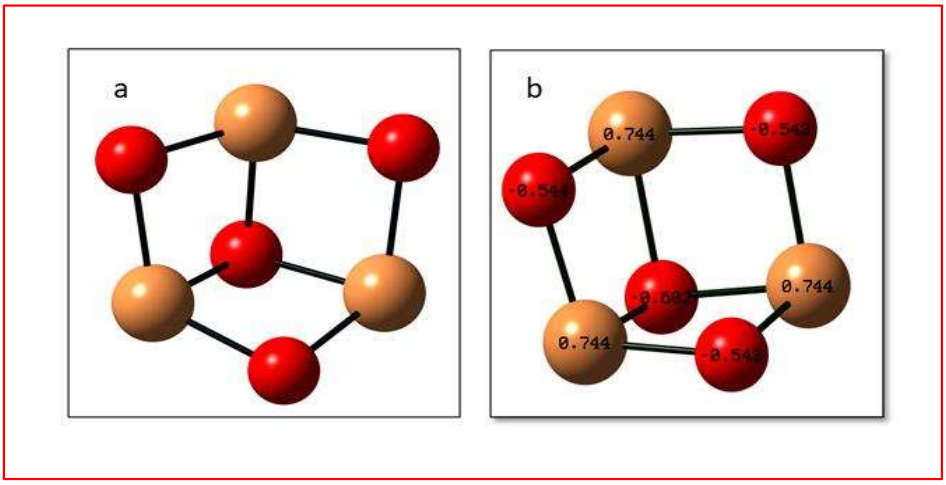

Figure 6.1 a) Initial Fe_3O_4 unit b) Optimized model of Fe_3O_4 unit with Mulliken charges.

Figures 6.1b displays the optimized Fe_3O_4 model structure. This Fe_3O_4 unit was then placed at a distance of 3Å directly above the middle of the GO1 sheet and subjected to ground state optimization using the same combined basis sets and functional as earlier under unrestricted spin conditions of the Gaussian 16 program. TD-DFT calculations were also conducted on the final optimized GO1-Fe_3O_4 model using the identical basis set and functional [Nakata et al. (2006)]. All calculations were done in the gas phase. The TD-DFT calculations gave the excitation energies and the UV-visible spectrum. The Mulliken charges of each atom in the model were obtained from the Mulliken population analysis. NBO analysis was also performed to find the interaction strength between the graphene oxide functional group and the Fe_3O_4 unit.

6.3.2 Classical Molecular Dynamics Simulations

All the initial models used in the MD simulation were made on the MAPS (version 4.1.1) software. The unit cell of magnetite (crystallographic information file database number: 9007645) [Fleet (1981)] was multiplied to make a supercell. Then a magnetite cluster (shown in figure 6.2a) of 16 Å diameter (consisting of 203 atoms) was carved out of this supercell. This cluster was placed and fixed at the center of a cubical simulation

box of 75Å edge length. Four optimized GO1 model sheets were then placed on the magnetite cluster surface in a non-overlapping fashion. The MGOC abbreviation represents this model in the rest of the chapter. The model was then subjected to a one nanosecond NVT ensemble simulation for obtaining the stabilized MGOC cluster (Figure 6.2b). The PNP and H_2O_2 molecule models were initially made on the MAPS platform and then optimized by the MNDO method.

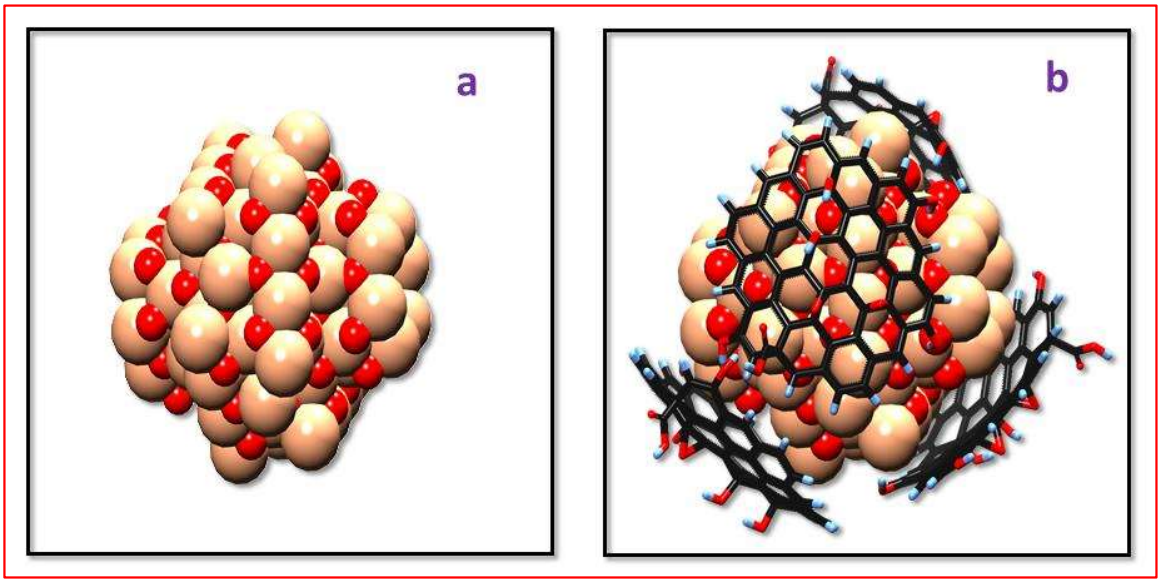

Figure 6.2 a) Magnetite cluster (total 203 atoms) and b) model of Magnetite-Graphene oxide nanocluster (MGOC).

Table 6.1 Charges on water model used in the simulations.

Atom type	Charge
OW	-1.040
HW	0.520

The TIP4P model H-O-H bond angle (Table 6.1) was the first input for constructing the three-site water model (model also used in chapter 4) used in this investigation. Then the TIP4P model fictitious site (M) charge (-1.04) was put on the O of three-site water model. The H atoms of the three-site model were given the same charge as H atoms in the TIP4P model. The empty space in the simulation box was uniformly filled with 30 PNP, 100 H_2O_2, and 2000 water molecules. This initial model was subjected to conjugate gradient optimization and a one nanosecond NPT ensemble MD simulation run. After the previous step, the liquid phase density surrounding the MGOC cluster was approximately 1g/cc. Lastly, the system was subjected to a canonical (NVT) ensemble MD simulation for 20 nanoseconds with a time step of 1 femtosecond. The first ten nanoseconds run were for equilibrating the system, while the last ten nanoseconds were for the production run. These simulations were carried out under periodic boundary conditions. The MD simulations were executed with the LAMMPS [Plimpton (1995)] program. Table 6.2 gives the details of the SciPCFF force field (modified version of PCFF based on 9-6 LJ potential) parameters used in the simulation [Sun et al. (1994)]. The Nosé-Hoover thermostat [Nosé (1984), Hoover, (1985)] controlled the temperature of the simulated system at 298 K using a ten femtosecond damping. A 12Å cut-off was used for nonbonded interactions, and the particle mesh approach calculated Coulomb interactions.

Table 6.2 LJ 9-6 Potential Parameters used in MD simulations.

Atom type	ϵ_0 **(kcal/mol)**	r_0 (Å)
cp (carbon attached to benzene ring in PNP)	0.119	3.426
n3o(Nitrogen atom of nitro group present in PNP)	0.081	3.28
ON (Oxygen atom of nitro group present in PNP)	0.081	2.97
OW (Oxygen atom in water)	0.15	3.15
Fe (Iron atom in magnetite)	0.83	3.56
O (Oxygen atom in magnetite)	0.132	3.168
hc (hydrogen attached to carbon atom in PNP)	0.038	2.51
oh (Oxygen atom of OH group in PNP)	0.162	3.172
oh (Oxygen atom of OH group in GO1)	0.162	3.172
ho (Hydrogen atom of OH group in PNP)	0.0135	0.949
ho2(hydrogen atom of COOH group in the GO1)	0.02	0.96
c_1 (carbon atom attached COOH group in the GO1)	0.20	3.32
o_2 (oxygen atom attached COOH group in the GO1)	0.40	2.88

6.4 Results and Discussion

6.4.1 Characterization

Figures 6.3a, 6.3b, and 6.3c show the XRD patterns of GO, magnetite, and MGO samples. The GO sample displays a peak at 2θ is equal to 10.2°. All peaks in the XRD's of magnetite and MGO matched those in the magnetite JCPDS file number 19-0629. The intensity of the GO peak relative to those of magnetite is quite low and hence not visible in the XRD of the composite. The 2θ peaks at 18.2°, 30.0°, 35.4°, 43.3°, 53.5°, 57.0°, 62.5° in the composite (Fig. 6.3c) XRD can be assigned to magnetite (111), (220), (311), (400), (422), (511) and (440) planes respectively.

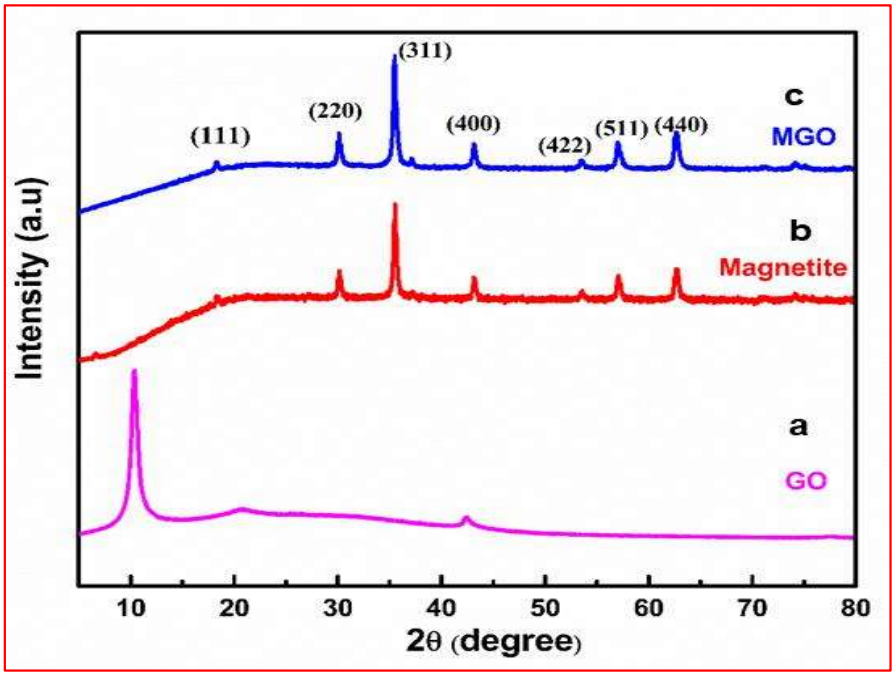

Figure 6.3 The XRD patterns of GO (a) and Magnetite (b) and MGO samples (c).

Figure 6.4 displays the FTIR spectra of GO, magnetite, and MGO samples. The peaks in the GO sample are at 1054 $cm^{-1,}$ and 1225 cm^{-1} is due to the epoxy and alkoxy bending vibrations of C-O atoms. Other peaks at 1372 cm^{-1} and 3401 cm^{-1} are assigned to the stretching -OH and bending vibrations of -C-O-H, respectively. The last two GO

peaks at 1620 cm^{-1} and 1730 cm^{-1} appear because of C-C and C=O (carbonyl) stretching vibrations. Both magnetite and MGO FTIR display a peak at 580 cm^{-1} due to the Fe-O (magnetite) vibration [Wang et al. (2013)]. New peaks obtained in the MGO sample at 1204 cm^{-1} and 1576 cm^{-1} confirm the interaction of iron of magnetite with GO atoms through COOH and C=C bonds [Wang et al. (2013)].

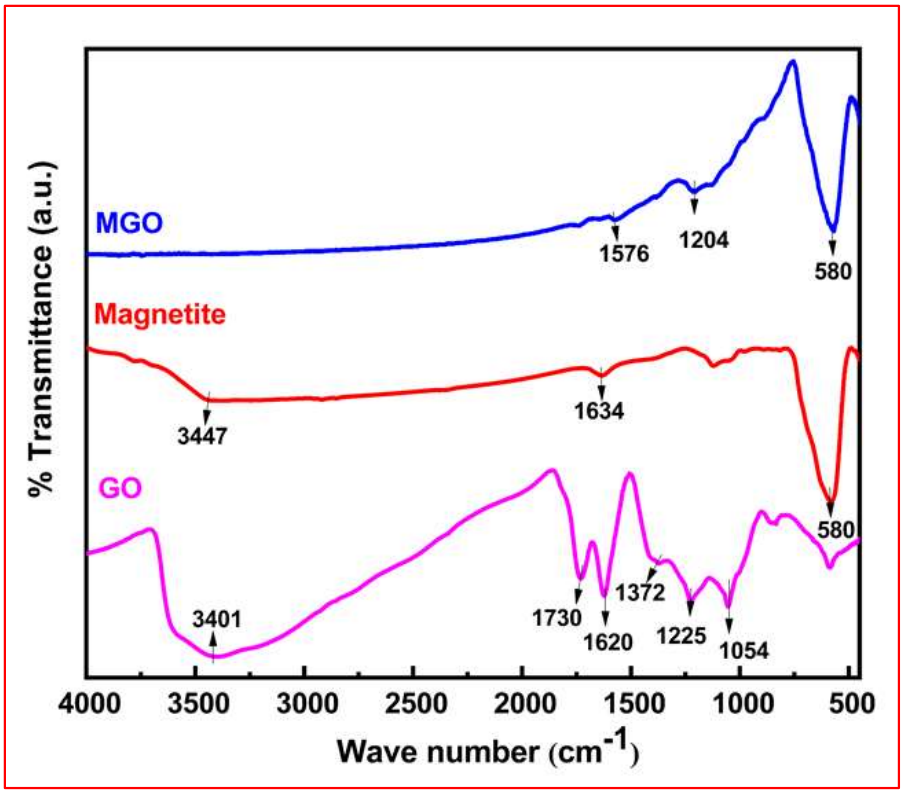

Figure 6.4 FTIR spectra of GO and Magnetite, MGO samples.

TEM images (Figure 6.5) show the morphology of GO and MGO nanocomposites. Figure 6.5a (TEM micrograph of GO) shows GO sheets are stacked together. The TEM images of the MGO sample (figure 6.5b) display magnetite nanoparticles embedded on the GO nanosheets. This figure reinforces the strong GO-magnetite FTIR interaction evidence. The inset figure 6.5b shows the size distribution of

the magnetite nanoparticles deposited on GO sheets. The size of magnetite nanoparticles deposited on the GO surface was in the 8 to 9 nm [Wan et al. (2007)] range.

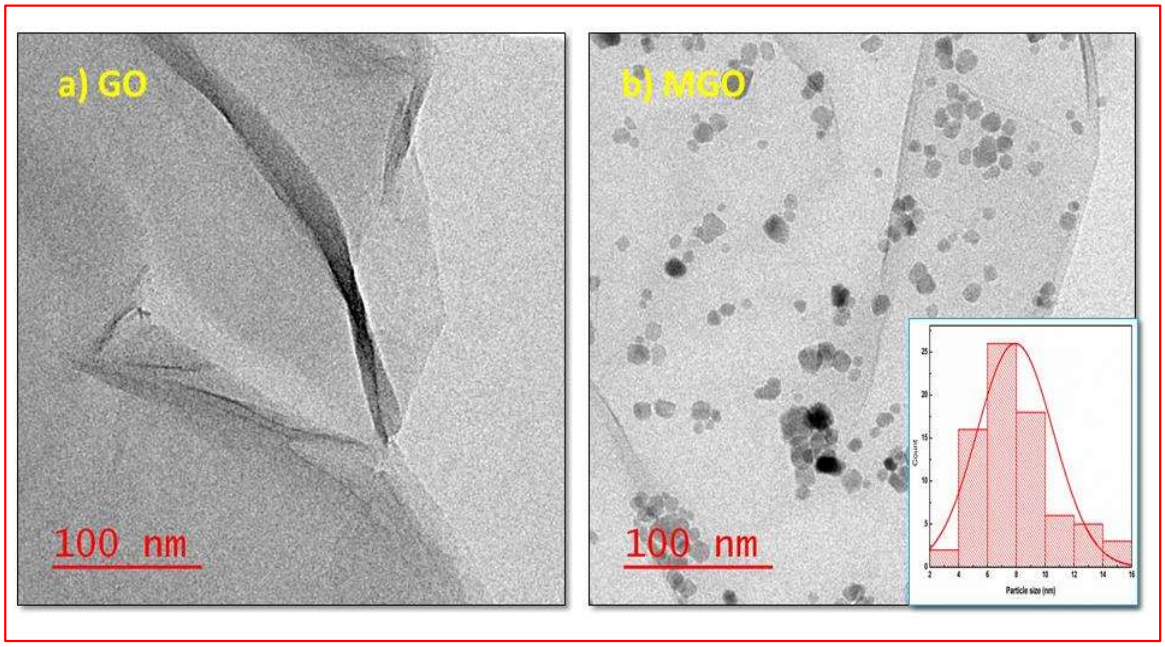

Figure 6.5 TEM images of a) GO and b) MGO samples. The inset figure shows the size distribution of loaded magnetite nanoparticles over the GO sheets.

Figure 6.6 depicts the direct bandgaps of GO and magnetite. The bandgap is calculated by the Tauc plot relation [Kumar et al. (2019)]. The band gaps of the GO and the magnetite samples were 2.0 eV and 1.8 eV, respectively.

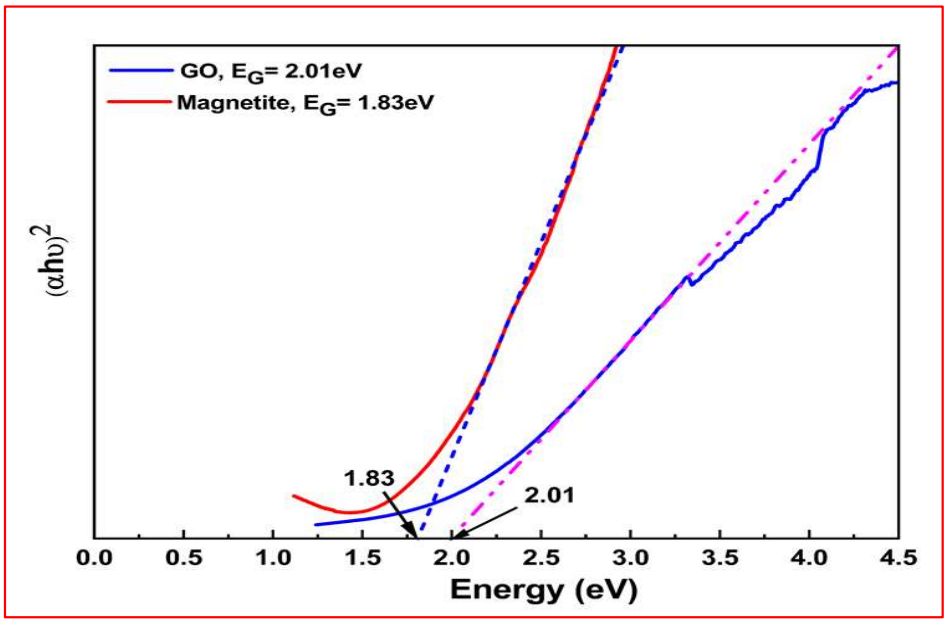

Figure 6.6 Tauc plots for direct bandgap for GO and Magnetite samples.

6.4.2 Photo-Fenton experiment analysis

Figures 6.7a and 6.7b exhibit the UV-visible spectra for Fenton and photo-Fenton degradation of PNP over the MGO catalyst with reaction time. Complete PNP degraded in 200 minutes over MGO under acidic Fenton conditions (Figure 6.7a). The same PNP concentration got completely degraded in 90 minutes (Figure 6.7b) under visible light irradiation (photo-Fenton conditions). Furthermore, all peaks in the UV-visible spectrum of PNP disappeared with degradation, showing that PNP degraded into small fragments with no UV-visible signature.

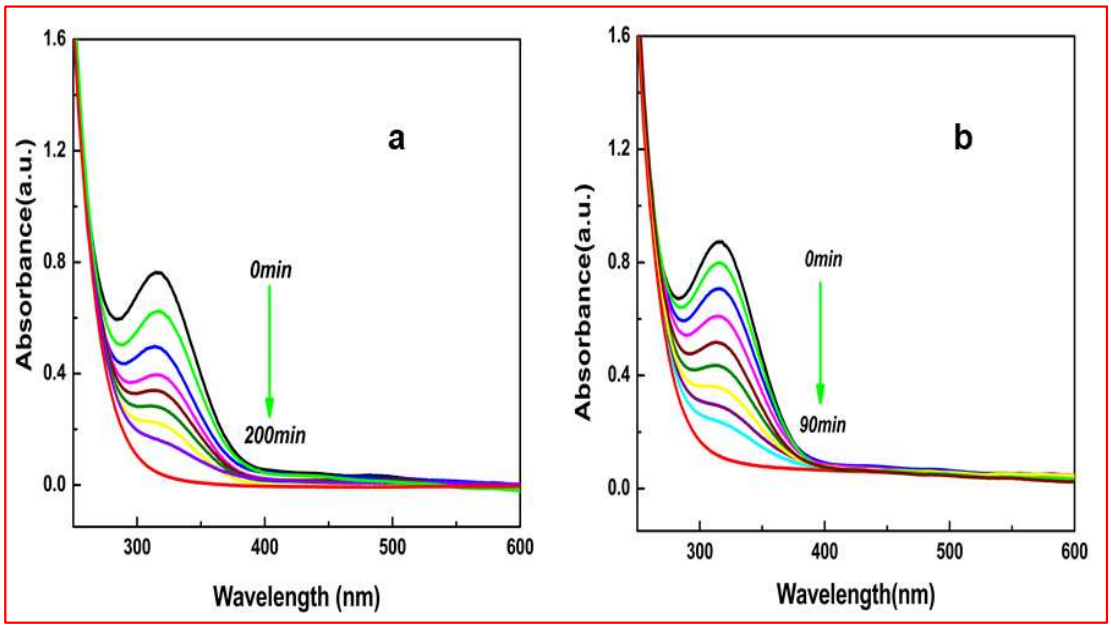

Figure 6.7 UV-visible plots for PNP degradation under (a) Fenton (in dark conditions) and (b) photo-Fenton (visible light condition) with reaction time under optimum reaction conditions over MGO sample**.**

Figure 6.8a shows the kinetics plots of Fenton and photo-Fenton catalytic degradation of PNP on GO, magnetite, and MGO samples. Fenton degradation (in the dark) of PNP on MGO followed pseudo-first-order rate kinetics. But visible light photo-Fenton PNP degradation followed pseudo-zero-order kinetics. In both plots C_o represents the initial concentration of PNP at time t = 0, and C is the final concentration of PNP at time t. The slope of the linear fit to the $ln\left(\frac{C}{C_o}\right)$ versus t graph gave the first-order rate constant. Similarly, the slope of the linear fit to the $\left(\frac{C}{C_o}\right)$ versus t plot gave the rate constant for photo-Fenton PNP degradation over MGO (Fig. 6.8b). The rate constant for MGO is greater than GO and magnetite samples under both Fenton and photo-Fenton conditions. No comparison between the Fenton and photo-Fenton rate constants can be made because of the different degradation kinetics orders.

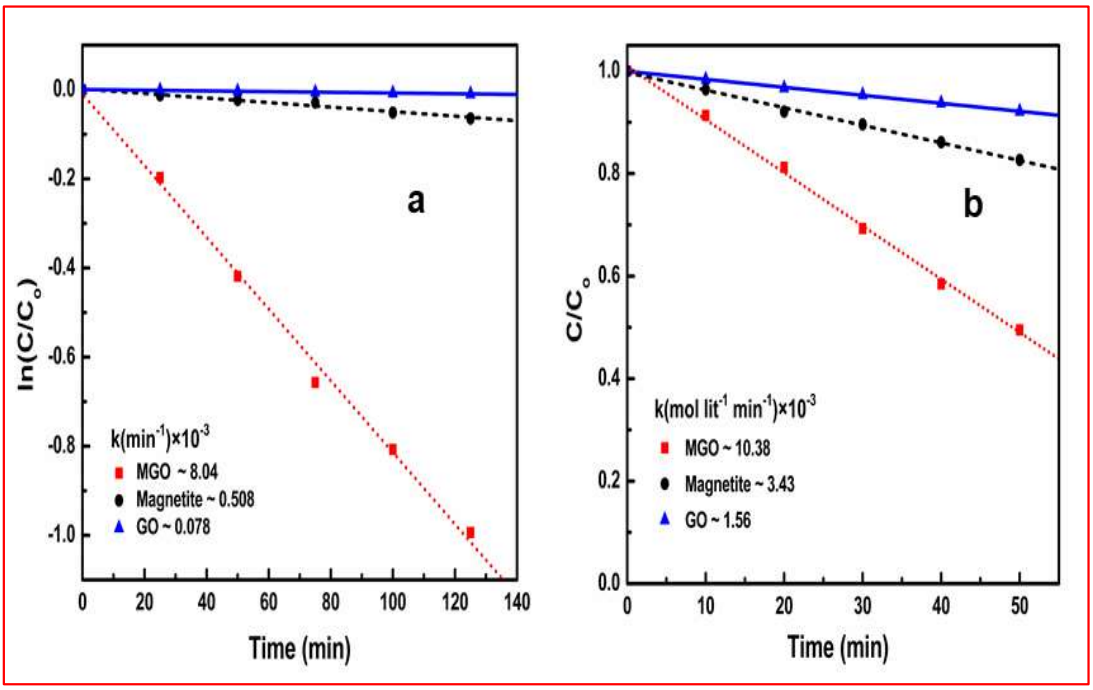

Figure 6.8 Catalytic kinetics plots of PNP degradation on MGO under (a) Fenton (in dark conditions) and (b) photo-Fenton (under visible light (14W) irradiation) conditions.

Activities of photocatalysts exhibiting different kinetics can be compared using turnover frequency (TOF). Thus, the TOF values for PNP degradation kinetics under the Fenton and photo-Fenton conditions were calculated using the equation given below [Kumar et al. (2019)].

$$TOF = \frac{Number\ of\ moles\ of\ reactant \times yield}{Number\ of\ grams\ of\ catalyst \times time\ (minute)}$$

Table 6.3 TOF values over Magnetite and MGO catalysts under Fenton and photo-Fenton conditions for PNP degradation.

PNP degradation for Fenton		
Catalyst	**Time(minutes)**	**TOF (moles gram^{-1} min^{-1})**
Magnetite	125	1.06×10^{-8}
MGO	125	1.08×10^{-7}
PNP degradation for photo-Fenton, Light source: 14W cool white LED		
Magnetite	50	7.45×10^{-8}
MGO	50	2.17×10^{-7}

The TOF values for Fenton degradation was 1.08×10^{-7} moles gram^{-1} min$^{-1,}$ and for photo- Fenton was 2.17×10^{-7} moles gram^{-1} min^{-1} over MGO. Hence, the TOF value doubled for the reaction under photo-Fenton conditions.

6.4.3 Recyclability test

The recyclability of the MGO sample was investigated under visible light irradiation (or photo-Fenton) conditions (Figure 6.9a). The MGO sample was stable during the PNP degradation process and could be reused until the 5th cycle (Figure 6.9a). The catalyst activity got reduced to only 87% of that observed in the first cycle. Magnetic decantation was used to recover the MGO sample after each cycle of catalysis quickly (Figure 6.9b).

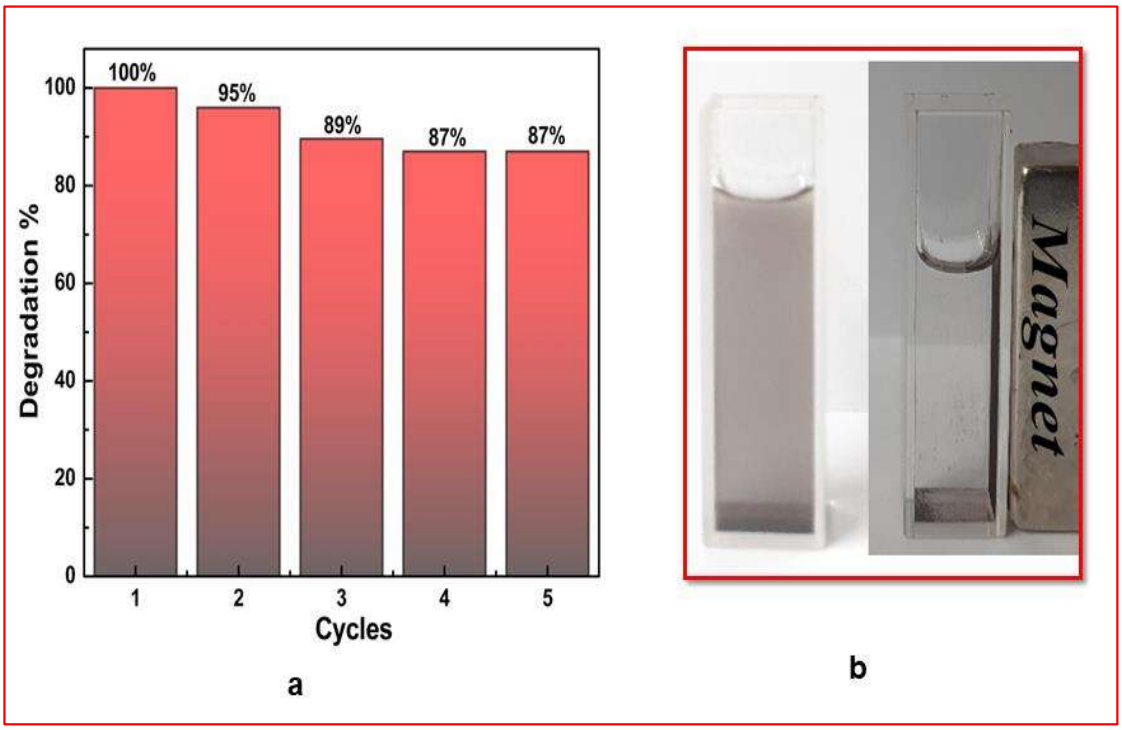

Figure 6.9 a) MGO recyclability results in histogram format for photo-Fenton PNP degradation at pH 3. b) The picture shows the magnetic recovery of the MGO sample after catalysis.

6.4.4 Computational analysis

Figure 6.10 shows the optimized structure of the GO1-Fe_3O_4 composite model.

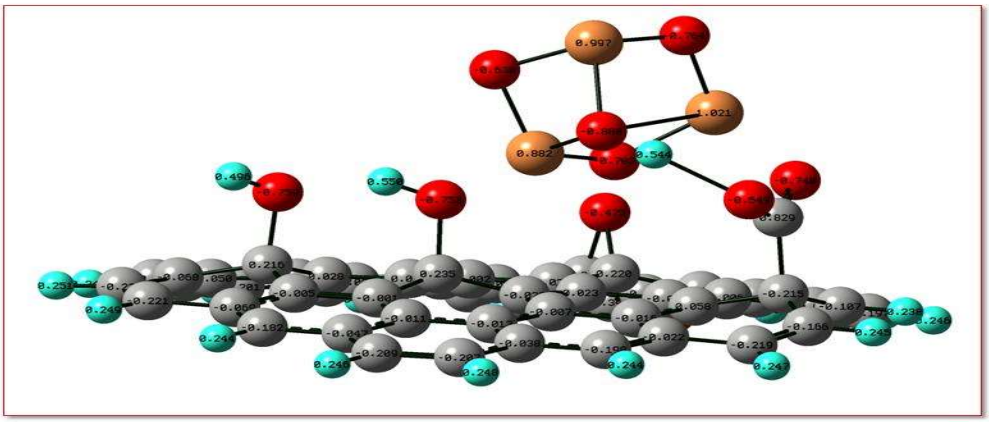

Figure 6.10 The optimized structure of the GO1-Fe_3O_4 model with Mulliken charges.

The following formula calculated the interaction energy of the GO1-Fe_3O_4 composite model.

Interaction energy = PE (GO1-Fe_3O_4)- [PE (GO1) + PE (Fe_3O_4 unit)] (6.1)

Where, PE = Potential energy

Table 6.4 The Potential energy of optimized model Fe_3O_4, GO1 and GO1-Fe_3O_4.

Potential energy (Hartree)		
Fe_3O_4 unit	**GO1 optimized model**	**GO1-Fe_3O_4 optimized model**
-670.3 1	-2560.01	-3230.53

The negative interaction energy (-0.22 Hartree) between the Fe_3O_4 and the GO models shows the stability of the composite. The charges found in the optimized Fe_3O_4 unit; all Fe atoms contains symmetrical charge distribution (+0.744). After interaction of Fe_3O_4 unit with GO1 model, the charges on Fe atoms became unsymmetrical (+0.882 to +1.021). Furthermore, an NBO analysis of the composite yielded a better understanding of the interaction chemistry between the Fe_3O_4 and the GO models.

6.4.4.1 Natural Bonding Orbital (NBO) Analysis

The following equation gives the expression for the stabilization (or interaction) energy E(2) associated with delocalization of electron pair from donor (NBO) orbital (i) to acceptor (NBO) orbital (j) [Reed et al. (2002)].

$$E(2) = q_i \frac{F_{ij}^2}{\epsilon_i - \epsilon_j} \quad (6.2)$$

Here, q_i is the orbital donor population,

ϵ_i represents the orbital energy of the donor NBO orbital,

ϵ_j is the orbital energy of the acceptor NBO orbital,

F_{ij} is the Kohn–Sham matrix elements between *i* and *j* NBO orbitals.

Below Table 6.5 summarizes the NBO calculation results, showing that the OH groups in GO interact strongly with Fe in the Fe_3O_4 cluster.

Table 6.5 Significant donor-acceptor NBO interactions between Fe_3O_4 unit and GO sheet model with the second-order stabilization energies E(2) kcal/mol.

Donor(i)	Acceptor(j)	E(2) for interaction kcal/mol
221.LP(2)O76 (OH group in GO)	253.LP*(4)Fe87	21.35
221.LP(2)O76 (OH group in GO)	255.LP*(6)Fe87	9.77
216.LP(2)O73 (COOH group in GO)	238.LP*(5)Fe85	9.31
215.LP(1)O73 (COOH group in GO)	237.LP*(4)Fe85	9.11
9.BD(1)C3-O76 (carbon attached with OH group in GO)	255.LP*(6) Fe87	1.70
118.BD(1)O76-H77 (OH group in GO)	255.LP*(6)Fe87	2.09
114.BD(1)C72-O73 (COOH group in GO)	240.LP*(7)Fe85	2.17

6.4.4.2 TD-DFT calculations

For a deeper understanding of the excited state of the MGO composite, TD-DFT calculations were also performed on the ground state model of GO1-Fe_3O_4 (Figure 6.10).

The functional (B3LYP) and the basis sets were the same as ground state optimization. Figure 6.11 exhibits the simulated absorption spectra of the GO1-Fe_3O_4 composite model in terms of oscillator strength. The electronic transitions excitations at different wavelengths are shown by vertical lines. Figure 6.11 also displays the experimental UV-visible spectrum of the MGO nanocomposite that has a broad peak in the range of 300-415 nm. The experimental absorbance data were measured in the solution phase, whereas the calculated data were in the gaseous state.

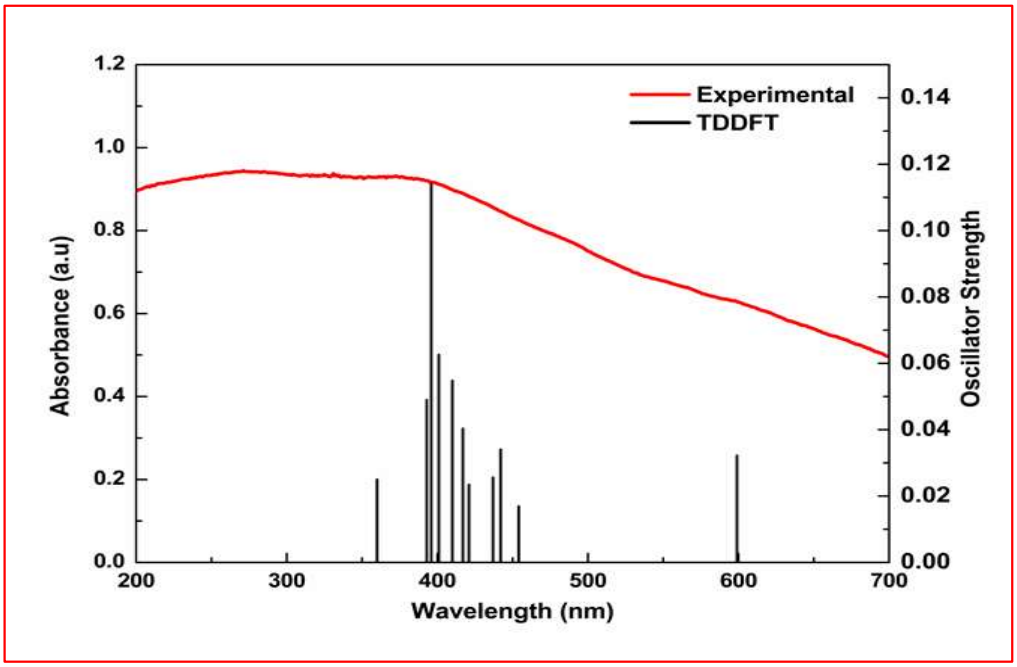

Figure 6.11 Experimental (red plot) shows UV-visible absorption spectrum of MGO sample and TD-DFT (black plot) shows calculated UV-visible absorption spectrum of GO1-Fe_3O_4 model.

6.4.4.3 HOMO-LUMO orbital analysis in DFT and TD-DFT calculations

Frontier molecular orbital theory analysis gives the HOMO, and LUMO locations on the GO1-Fe_3O_4 composite (Figure 6.12). This analysis was executed on the optimized

ground (DFT) and the excited state (TD-DFT) composite structure. The TD-DFT HOMO-LUMO analysis was implemented on the 410 nm excited state. In the ground state, the HOMO is mainly on the benzene rings and the epoxy groups of GO. At the same time, the LUMO is localized partly on some benzene rings and hydroxyl groups of GO. After photo-excitation, the HOMO shifted partly from the GO benzene rings to Fe and O atoms of the Fe_3O_4 unit. A red circle in Figure 6.12 has demarcated the discussed portion. Thus, photo-excitation transfers charge from the GO portion to the magnetite part.

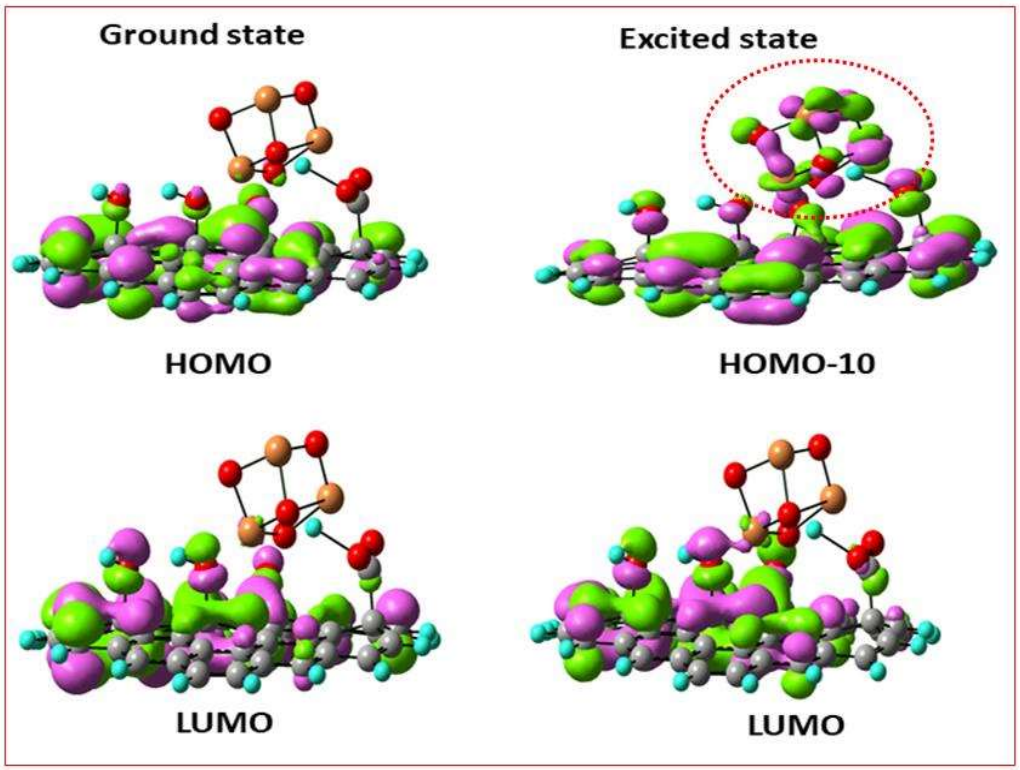

Figure 6.12 HOMO/LUMO (beta spin) (ground state and excited state (410nm)) obtained by DFT and TD-DFT calculation.

6.4.4.4 MD results

Figure 6.13 shows a snapshot of the system at the end of a long MD equilibration run, which describes the distribution of H_2O_2 and PNP molecules around the MGOC cluster. But this snapshot does not give the H_2O_2 or PNP location relative to the GO or magnetite parts of the composite.

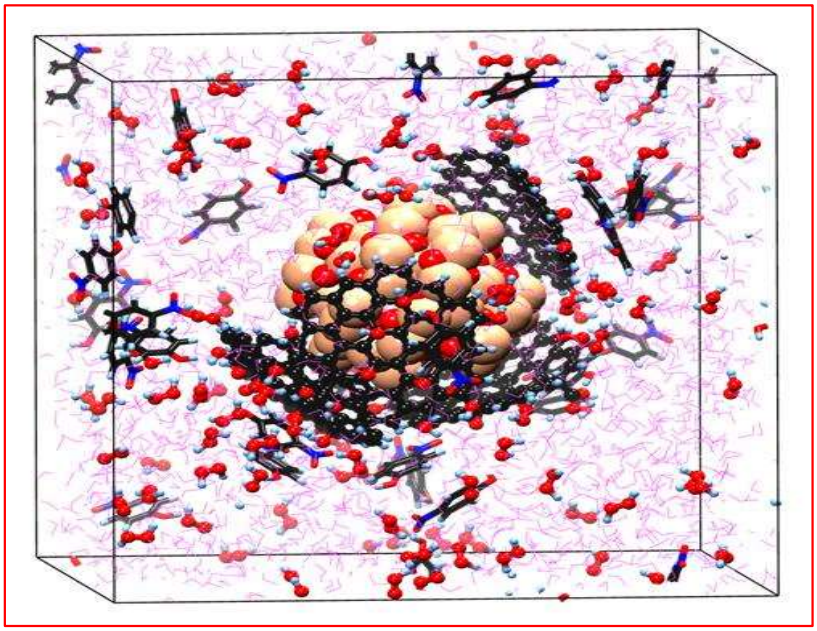

Figure 6.13 Snapshot showing the distribution of H_2O_2 and PNP around the GOMC cluster.

The center of mass RDF (COM-RDF) gives a more quantitative view of this situation. Figure 6.14a shows the long-time average COM-RDF for H_2O_2 and PNP from the center of the GOMC cluster. The peak of GOMC-H_2O_2 appears to start about at 8 Å. In contrast, the most probable distance between GOMC and PNP molecules is ~12 Å. The GOMC-H_2O_2 peak position indicates that the interaction between GOMC and H_2O_2 molecules is stronger than between GOMC and PNP. As mentioned earlier in Chapter 4, the H_2O_2 molecules (in an aqueous solution of PNP) interact less favorably with a bare

magnetite cluster. Hence, making a magnetite-graphene oxide composite improves H_2O_2 affinity towards the catalyst.

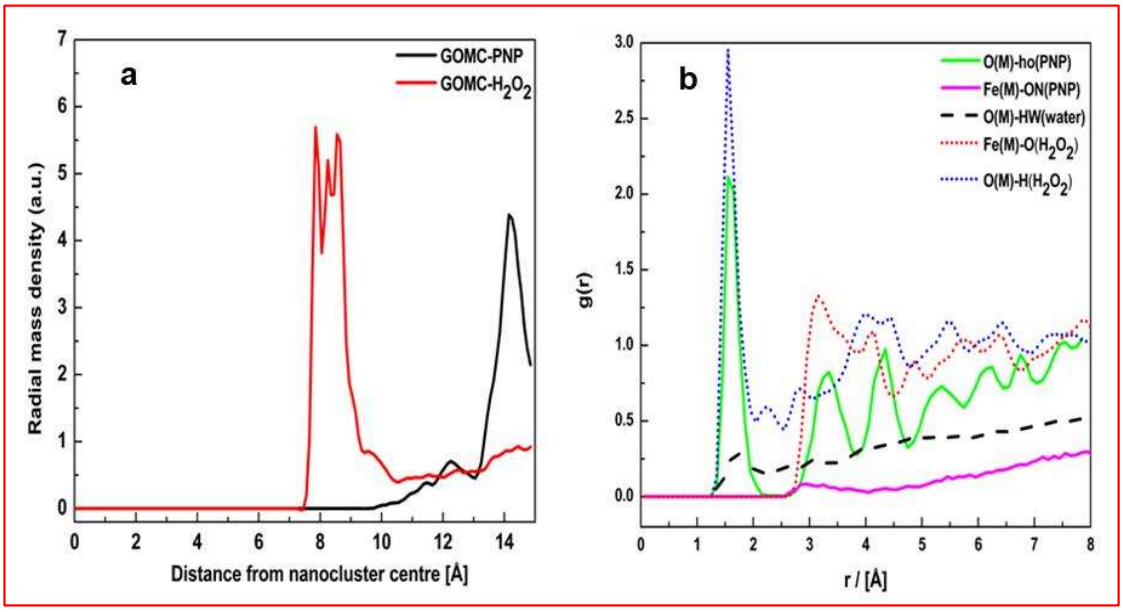

Figure 6.14 a) RDF-COM profiles of H_2O_2 and PNP from the center of GOMC, b) RDF plots show the interaction of atoms in PNP, water, and H_2O_2 with those constituting the GOMC composite cluster, respectively. [The involved atom types are Fe(M): Iron of magnetite, O(M): oxygen of magnetite, ON: oxygen atom of the nitro group present in PNP, HW: hydrogen atom in water, ho: hydrogen atom of the OH group in PNP, O: oxygen atom in H_2O_2, H: hydrogen atom in H_2O_2]

The long-time average RDF gives the relative interaction strength between two different atom types. The RDF plots in Figure 6.14b depict the interaction of different atoms in the magnetite part of the composite with the atom types constituting PNP, water, and H_2O_2 molecules. The strongest (at 1.5Å) interaction is between the oxygen of magnetite and the hydrogen in H_2O_2 (blue dashed O(M)-H(H_2O_2) plot). The oxygen of magnetite also interacts with the hydroxyl group of PNP molecule at the same distance but with less intensity shown by solid green plot (O(M)-HO(PNP)). More importantly, there is a prominent RDF peak between Fe and the oxygen of H_2O_2 at ~3Å. This RDF

peak is significant because a Fenton reaction would involve electron transfer from the Fe atom of Fe_3O_4 to H_2O_2.

6.4.5 Mechanism

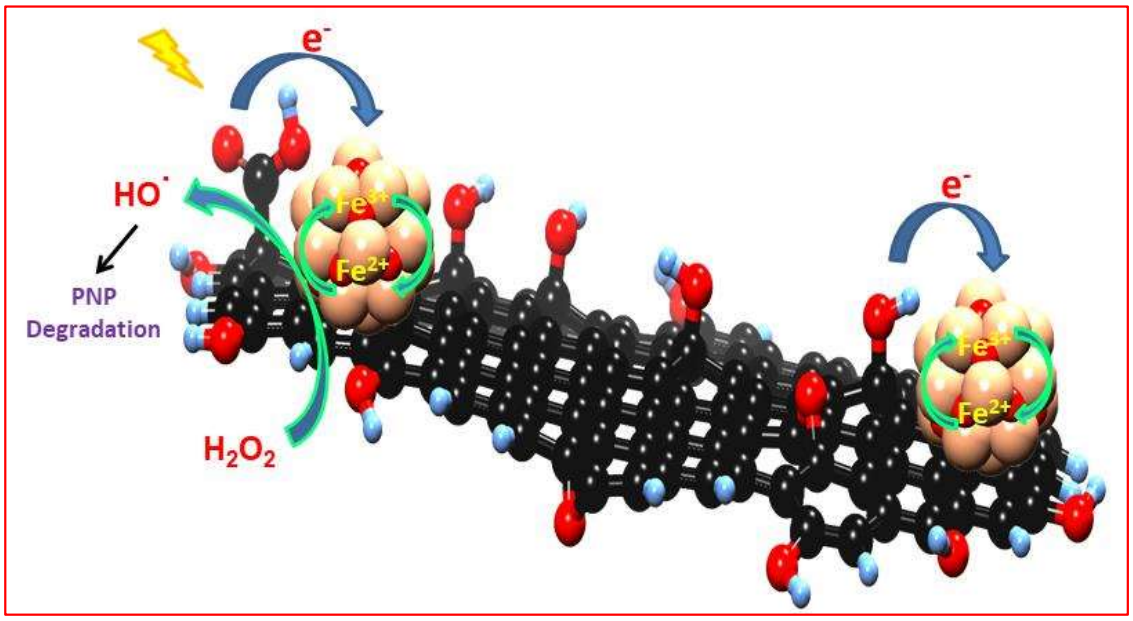

Figure 6.15 Photo-Fenton degradation mechanism of PNP on the MGO nanocomposite.

This section combines the experimental, DFT, and MD simulation results to arrive at the probable Fenton and photo-Fenton mechanisms. The ground state DFT calculations show that predominantly HOMO resides on the GO part. At the same time, MD simulations give the information that H_2O_2 interacts better with the GOMC surface than a bare magnetite cluster. Nevertheless, there is very little of the HOMO of the GOMC on the Fe atoms of the magnetite part. In contrast, visible light irradiation shifts the HOMO of the composite to the magnetite part and makes it electron-rich or nucleophilic. In addition to the preceding, the increased affinity of H_2O_2 (MD simulation results) towards the MGOC surface enhances the photo-Fenton hydroxyl radical generation efficiency. Figure 6.15 illustrates this mechanism for the GOMC model.

6.5 Conclusions

The heterogeneous photo-Fenton reaction mechanism of PNP degradation is examined on the surface of MGO nanocomposites. The experimental results show that the TOF value for the visible light photo-Fenton degradation of PNP is double of the Fenton reaction (dark) activity for the same substrate. Furthermore, PNP degradation follows first-order kinetics in the absence of light and pseudo-zero order kinetics on visible light irradiation over MGO catalyst, implying different reaction mechanisms in the Fenton and photo-Fenton cases. The COM-RDF from MD simulations shows that H_2O_2 molecules are closer than PNP to the GOMC surface. The DFT and TD-DFT calculations show that photo-excitation shifts the HOMO from the GO part to the magnetite cluster. In particular, there is (NBO analysis) electron transfer from the oxygen atom of the OH group (as donor) in the GO part to the iron atom in the Fe_3O_4 (as acceptor) portion of the composite. Thus, the photo-excitation of the MGO composite makes its magnetite part more nucleophilic, increasing its H_2O_2 reduction potency for $^{\bullet}OH$ generation.